

Contents

1	Introduction	3
2	Trigger implementation at LOFAR	5
2.1	Data flow	6
3	Filtering	7
3.1	Narrowband radio frequency interference mitigation	8
3.2	Optimum window	9
3.3	Frequency filter and pulse structure	11
3.4	Noise with different filtering methods	12
4	Pulse-search algorithm	13
4.1	Power of N consecutive time samples (P_N)	14
4.2	Accidental noise pulses & threshold determination	14
4.3	Pulse amplitude distribution	15
4.4	Detection efficiency	18
5	Ionospheric dispersion	20
6	Beaming	21
7	Energy limit of ultra high energy particle	24
8	Summary and conclusions	26
9	Acknowledgements	26
	Appendix A The polyphase filter and inversion	27

Optimized Trigger for Ultra-High-Energy Cosmic-Ray and Neutrino Observations with the Low Frequency Radio Array

K. Singh^{a,b,c}, M. Mevius^a, O. Scholten^a, J.M. Anderson^d, A. van Ardenne^e, M. Arts^e, M. Avruch^{e,h}, A. Asgekar^e, M. Bell^f, P. Bennema^e, M. Bentum^e, G. Bernadi^{g,h}, P. Bestⁱ, A.-J. Boonstra^e, J. Bregman^e, R. van de Brink^e, C. Broekema^e, W. Brouwe^e, M. Brueggen^j, S. Buitink^{k,l,b}, H. Butcher^{e,m}, W. van Cappellen^e, B. Ciardiⁿ, A. Coolen^e, S. Damstra^e, R. Dettmar^o, G. van Diepen^e, K. Dijkstra^e, P. Donker^e, A. Doorduyn^e, M. Drost^e, A. van Duin^e, J. Eisloffel^p, H. Falcke^{k,e,d}, M. Garrett^e, M. Gerbers^e, J. Griessmeier^{e,q}, T. Grit^e, P. Gruppen^e, A. Gunst^e, M. van Haarlem^e, M. Hoeft^p, H. Holties^e, J. Hörandel^k, L.A. Horneffer^{d,k}, A. Huijgen^e, C. James^k, A. de Jong^e, D. Kant^e, E. Kooistra^e, Y. Koopman^e, L. Koopmans^h, G. Kuper^e, P. Lambropoulos^{e,h}, J. van Leeuwen^e, M. Loose^e, P. Maat^e, C. Mallery^a, R. McFadden^e, H. Meulman^e, J.-D. Mol^e, J. Morawietz^e, E. Mulder^e, H. Munk^e, L. Nieuwenhuis^e, R. Nijboer^e, M. Norden^e, J. Noordam^e, R. Overeem^e, H. Paas^r, V.N. Pandey^h, M. Pandey-Pommier^{h,s}, R. Pizzo^e, A. Polatidis^e, W. Reich^d, J. de Reijer^e, A. Renting^e, P. Riemers^e, H. Roettgering^t, J. Romein^e, J. Roosjen^e, M. Ruiter^e, A. Schoenmakers^e, G. Schoonderbeek^e, J. Sluman^e, O. Smirnov^e, B. Stappers^u, M. Steinmetz^v, H. Stiepel^e, K. Stuurwold^e, M. Tagger^q, Y. Tang^e, S. ter Veen^k, R. Vermeulen^e, M. de Vos^e, C. Vogt^e, E. van der Wal^e, H. Weggemans^e, S. Wijnholds^e, M. Wise^e, O. Wucknitz^w, S. Yattawatta^h, J. van Zwieten^e

^a*Kernfysisch Versneller Instituut, University of Groningen, 9747 AA Groningen, The Netherlands*

^b*Vrije Universiteit Brussel, Dienst ELEM, B-1050 Brussels, Belgium*

^c*Department of Physics, University of Alberta, Edmonton, AB, T6G 2G7, Canada*

^d*Max-Planck-Institut für Radioastronomie, Auf dem Hügel 69, 53121 Bonn, Germany*

^e*ASTRON, Oude Hoogeveensedijk 4, 7991 PD Dwingeloo, The Netherlands*

^f*School of Physics and Astronomy, University of Southampton, Southampton, SO17 1BJ, UK*

^g*Center for Astrophysics, Harvard University, USA*

^h*Kapteyn Astronomical Institute, PO Box 800, 9700 AV Groningen, The Netherlands*

ⁱ*Institute for Astronomy, University of Edinburgh, Royal Observatory of Edinburgh, Blackford Hill, Edinburgh EH9 3HJ, UK*

^j*Jacobs University Bremen, Campus Ring 1, 28759 Bremen, Germany*

^k*Department of Astrophysics, IMAPP, Radboud University Nijmegen, 6500 GL Nijmegen, The Netherlands*

^l*Lawrence Berkeley National Laboratory, Berkeley, California 94720, USA*

^m*Mt Stromlo Observatory, Research School of Astronomy and Astrophysics, Australian National University, Weston, A.C.T. 2611, Australia*

ⁿ*Max Planck Institute for Astrophysics, Karl Schwarzschild Str. 1, 85741 Garching, Germany*

^o*Astronomisches Institut der Ruhr-Universität Bochum, Universitätsstrae 150, 44780 Bochum, Germany*

^p*Thüringer Landessternwarte, Sternwarte 5, D-07778 Tautenburg, Germany*

^q*Laboratoire de Physique et Chimie de l'Environnement et de l'Espace 3A, Avenue de la Recherche Scientifique 45071 Orleans cedex 2, France*

^r*CIT, University of Groningen, The Netherlands*

^s*Centre de Recherche Astrophysique de Lyon, Observatoire de Lyon, 9 av Charles Andr, 69561 Saint Genis Laval Cedex, France*

^t*Leiden Observatory, Leiden University, PO Box 9513, 2300 RA Leiden, The Netherlands*

^u*Jodrell Bank Center for Astrophysics, School of Physics and Astronomy, The University of Manchester, Manchester M13 9PL, UK*

^v*Astrophysikalisches Institut Potsdam (AIP), An der Sternwarte 16, 14482 Potsdam, Germany*

^w*Argelander-Institute for Astronomy, University of Bonn, Auf dem Huegel 69, 53121, Bonn, Germany*

Abstract

When an ultra-high energy neutrino or cosmic ray strikes the Lunar surface a radio-frequency pulse is emitted. We plan to use the LOFAR radio telescope to detect these pulses. In this work we propose an efficient trigger implementation for LOFAR optimized for the observation of short radio pulses.

Keywords: Ultra-High Energy Cosmic Rays, Ultra-High Energy Neutrinos, Lunar Radio Detection, Nano-Second Pulse Detection, LOFAR, Frequency Filter detection

PACS: 95.55.-n, 95.55.Jz, 95.75.Wx, 95.85.Bh, 95.85.Ry

1. Introduction

Ultra-High Energy (UHE) cosmic-ray particles are a source of much speculation. Particles with more than 10^{20} eV of energy have been observed, but the source of these particles is an open question in astroparticle physics. Such energetic particles are extremely rare; their flux on Earth is less than $1 \text{ km}^{-2} \text{ century}^{-1}$. This low flux makes it difficult to determine the origin of these particles. They may be accelerated by shock waves in Active Galactic Nuclei (AGN) [1], but it is also possible that they are created by annihilating or decaying dark-matter particles [2]. We do know that these UHE cosmic rays will not be bent appreciably by the galactic magnetic field, because their high momentum gives them high magnetic rigidity. Furthermore, due to the GZK effect [3], the sources of the UHE cosmic rays we do detect have to be close to Earth, a distance of the order of 50 Mpc or less, as it prevents us from detecting UHE cosmic rays from distant sources.

There is an alternative approach to finding the sources of UHE cosmic rays. Instead of detecting the cosmic rays directly, we aim to detect the neutrinos that are produced at their creation sites or in transport through their interaction with the cosmic microwave background [3], known as the GZK effect. These neutrinos will carry most of the energy of the original cosmic ray, but are almost unaffected by the intergalactic medium, and thus carry direct information about the UHE cosmic rays from distant sources.

Because of their limited interactions, neutrinos are very difficult to detect. To measure the small flux of UHE neutrinos, it is necessary to use detectors with an extremely large acceptance. Such detectors include the Pierre Auger Observatory [4], ICECUBE [5], ANITA [6], FORTE [7] and KM3Net [8].

Celestial bodies can serve as large-acceptance detectors. In 1989, Dagkesamanskii and Zhelenznykh [9] proposed using the Askaryan effect [10] to measure the flux of UHE neutrinos impinging on the Moon. The Moon offers an acceptance area on the order of 10^7 km^2 , far larger than any man-made structure. Having such a large acceptance allows for sensitive measurements of the flux of these UHE neutrinos and cosmic rays. Based on Dagesamanskii and Zhelenznykh's concept, experiments have been carried out at the Parkes [11, 12], Goldstone [13], Kalyazin [14], and recently at the VLA [15] telescopes. These experiments have looked for short radio pulses near the frequency where the intensity of the Askaryan effect is expected to reach its maximum. It may be advantageous to look for pulses at lower frequencies, where the angular spread of the emission around the Cherenkov angle is larger. This results in an increase in detection sensitivity [16] for three reasons: for a much larger range of incident angles the radio

34 waves will reach Earth, internal reflection at the Lunar surface is of lesser importance, and the
35 absorption length increases, which means that the waves emitted by neutrino-induced showers
36 at greater depth will still be detectable. It was shown [16] that the optimum frequency-window
37 for this observation is around 100–200 MHz. To perform observations of narrow transients in
38 this frequency band a new program was initiated called NuMoon. Initially the Westerbork Syn-
39 thesis Radio Telescope (WSRT) has been used to make such observations at frequencies near 150
40 MHz. These observations have been used to improve the flux-limit for UHE neutrinos [17, 18]
41 by about an order of magnitude. We aim to further improve this result by using LOFAR (LOw
42 Frequency ARray) [19]. With LOFAR’s larger collecting area and wider frequency range, a 25
43 times higher sensitivity for the detection of UHE particles is within reach [42].

44 The main issue for the NuMoon observations with LOFAR is dealing with the high data
45 rate. The data rate of the raw time-series is about 1 TB/s. Even if only 1 ms of data is stored
46 per event, this still creates a high load on the data transmission lines and storage devices at
47 the CEntRAL Processor facility (CEP) and necessitates the implementation of a very efficient
48 trigger algorithm. It is crucial to reduce the number of false detection events, since a single
49 event consists of about 1.6 GB of data. The triggering criteria must be optimized so that false
50 detection events occur infrequently, but real events are not missed. It should be realized that
51 this last condition is essential since only the triggered data are stored and available for later
52 processing. If the trigger condition is too constraining, we would not be sensitive to pulses that
53 could easily be distinguished from a noise signal in an offline analysis using the full capability
54 of LOFAR. The construction of the trigger algorithm is the subject of this work.

55 The remote stations and the international stations of LOFAR (see Sec. 2) are important
56 to offline analysis of the detected events. There are two chief benefits to using remote and
57 international stations. One, because of the increased collecting area, the signal-to-background
58 ratio will be improved when these stations are used to form tied-array beams in an offline
59 analysis. Two, the pointing resolution of LOFAR is much better when well-separated stations
60 are contributing data because of the large interferometric baseline of these stations. Improved
61 pointing resolution increases the efficiency of the anti-coincidence criterion. It also gives better
62 information about the origins of genuine pulses. Knowing the place on the Moon where the
63 signal originates from allows for an accurate accounting of the Lunar terrain in simulations of
64 the signal.

65 The general structure of this paper is as follows, we start by presenting a general outline of
66 LOFAR in Sec. 2 with emphasis on the aspects which are relevant for the construction of the
67 trigger. For technical reasons, for the construction of an optimized trigger algorithm, only part
68 of the full band width may be used. In Sec. 3 we discuss the different alternatives for selecting
69 the part of the band that will be used. The pulse-search algorithm is presented in Sec. 4 in
70 conjunction with the procedure to optimize it. The signals arriving at the Earth from the Moon
71 pass through the ionosphere, which induces a dispersion that can be corrected for to a large
72 extent as discussed in Sec. 5. The complete simulation, including the effects of a distributed
73 antenna system, is presented in Sec. 6. In Sec. 7 the attainable flux limits are given for UHE
74 neutrinos and cosmic rays, given the sensitivity of the trigger algorithm.

75 2. Trigger implementation at LOFAR

76 LOFAR is a multi-purpose sensor array [20, 43] whose main application is radio astronomy.
77 As the name suggests, LOFAR is sensitive to low frequencies (10–240 MHz). It is a distributed
78 radio-interferometric array consisting of many low-cost antennas. These antennas are organized
79 into many separate array stations, and 40 of these stations are located in the northeastern
80 Netherlands. About half (24 when the array is completed) of these Dutch stations form the
81 “core” of LOFAR, and these core stations are clustered into an area 2 km in diameter. The
82 other 16 Dutch stations are called remote stations, and they are located within 80 km of the
83 core. Additionally, international stations have been constructed or are planned in various other
84 European countries. These countries include Germany, the UK, France and Sweden. The use of
85 the international stations gives LOFAR an interferometric baseline of approximately 1500 km.
86 The maximal interferometric baseline within the Netherlands is on the order of 100 km.

87 LOFAR works with two distinct antenna types, Low Band Antennas (LBA), which operate
88 between 10 and 80 MHz, and High Band Antennas (HBA), which operate between 110 and 240
89 MHz. In the present investigation, we are interested in the in the 110–190 MHz region of the
90 HBA antennas. These are bow-tie-shaped dual-dipole antennas, which are assembled in a 4X4
91 grid measuring 5 m×5 m. For each core station of LOFAR, the HBA antennas are grouped into
92 two sub-fields, each with 24 HBA-tiles and a diameter of 35 m. The distance between the two
93 groups is about 129 m. A remote station consists of a single group of 48 HBA-tiles. This group
94 has a total diameter of about 50m. An international station consists of a single group of 96
95 HBA-tiles with a total diameter of about 62 m.

96 The signals received by all antennas of a single HBA tile are added by an analogue beam-
97 former. Subsequently, the signals of all tiles of a single station are collected, and appropriate
98 phase-delays are applied to form the station beams. These digitally synthesized station beams
99 are equivalent to the beam of a single dish of a traditional radio telescope. Each LOFAR station
100 has a 10 Gbit/s connection to CEP with a real data rate between 3.2 Gbit/s per station. The
101 CEP is an IBM Blue Gene/P supercomputer and additional off-line clusters, located in Gronin-
102 gen, and is responsible for collecting and processing the data from the LOFAR stations. The
103 beams of the core stations are added in phase to form tied-array beams online at CEP [35, 36].
104 The use of tied-array beams improves the pointing resolution of LOFAR, since the core stations
105 have an interferometric baseline on the order of 2 km. In addition, tied array beam forming, by
106 summing station beams in phase, increases the effective area and thus the signal to noise ratio.

107 In parallel to this online data-processing, the digitized raw data of each tile are stored in ring
108 buffers, the Transient Buffer Boards (TBBs), at the station. The raw data stored in the TBBs
109 can be accessed for offline processing [42]. Each TBB stores the data from 8 dual polarized
110 tiles for 1.3s where there are advanced plans to extend this to 5.2s. The boards will upload
111 these data to CEP when triggered by the pulse detection software.

112 The observation mode of LOFAR to detect cosmic rays and neutrinos at energies above
113 10^{21} eV through their impacts on the Lunar surface is called the Ultra-High-Energy Particle
114 (UHEP)-mode or the NuMoon-mode. In this mode digital beams, pointing to different spots
115 on the Lunar surface, will be formed using all HBA fields ($24 \times 2 \times 24$ tiles) of the core stations
116 of LOFAR. These data will be searched for short pulses. When a pulse is found, a trigger is
117 sent to the TBBs. The raw data in the TBBs are then sent to CEP for storage and later offline
118 processing. This offline processing increases NuMoon’s sensitivity and reduces the occurrence

119 of false detection events.

120 *2.1. Data flow*

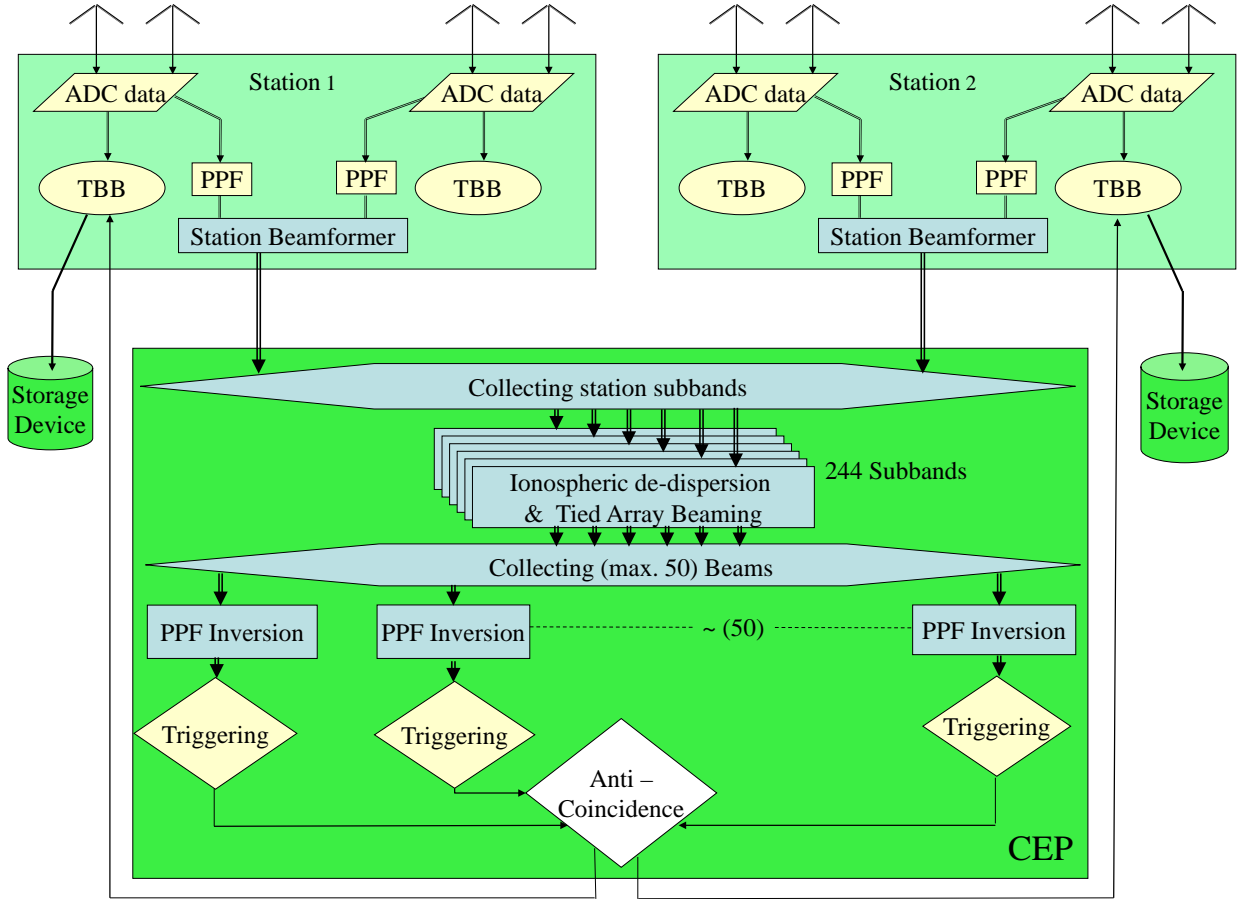


Figure 1: Online signal processing of LOFAR in the NuMoon pipeline [37].

121 The data flow through the system starting at the antennas is schematically depicted in Fig. 1.
 122 The main structures indicated are the many stations in the field, schematically shown by the
 123 two boxes in the upper half of the figure. Each station receives the signals from the HBA-tiles
 124 of the station where each HBA-tile contains 16 dual antennas. In the station electronics the
 125 analog signals of each tile are sampled at 200 MHz and converted to 12 bit digital samples. The
 126 digitized data are stored on a ring buffer for possible later processing. In addition the digitized
 127 signals are fed into a PolyPhase Filter (PPF) that also performs a Fast Fourier Transform
 128 (FFT) resulting in 512 frequency channels (subbands). The merits of the PPF are discussed
 129 in detail in the appendix. In the station beamformer the subbands of all tiles of a single
 130 HBA field are added in phase to form a single station beam. The phase-masks necessary for
 131 forming the station beams are recalculated by local control units every second for the source
 132 (the Moon) under observation. Each station beam is sent to CEP in the form of 244 frequency
 133 channels (subbands) as indicated by the heavy black arrows connecting the stations and CEP,
 134 corresponding to approximately half the available bandwidth.

135 At CEP the data of all stations are collected and a correction is applied to compensate for
136 the ionospheric dispersion of the signal. The massive parallel processing capability of CEP is
137 used to apply station-dependent phase shifts to form 50 tied-array beams for each of the 244
138 subbands. Simulations show that 50 tied-array beams are sufficient to cover the full Lunar
139 surface as discussed in Sec. 6. These 50 beams are aimed at different patches of the visible
140 Lunar surface. All the subbands of a single beam at a single computing node are then collected
141 and the data are transformed back into the time-domain. In this step, the effect of the PPF is
142 inverted (PPF inversion, see Appendix A).

143 Once the data have been converted back to the time-domain, each beam is searched for
144 suitable pulses. The design of an efficient search procedure is the main subject of this work.
145 In practice, many pulses will be due to transient noise. It is necessary to have an efficient
146 procedure to distinguish the noise pulses from genuine cosmic ray events (hereafter “genuine”
147 pulses will refer to events caused by cosmic ray and neutrino impacts on the Moon). We
148 can make use of the fact that genuine pulses come from a very localized spot on the Lunar
149 surface. A genuine pulse will thus be detected in one or at most a few adjacent beams. In
150 similar observations using the Westerbork Synthesis Radio Telescope [17, 18], as well as the
151 Parkes telescope [48], it has been found that putting an anti-coincidence requirement between
152 the beams is an efficient means of suppressing transient-noise triggers. The NuMoon pipeline
153 at LOFAR will incorporate such an anti-coincidence requirement in its triggering criteria. In
154 implementing this trigger, care must be taken with the side-lobe sensitivities of the beams which
155 are investigated in Sec. 6. Recall that triggering causes the TBBs to upload large amounts of
156 data to CEP and results in system dead time.

157 In our analysis, we have simulated each block in the data-processing chain of Fig. 1. In
158 this way, we estimate the total pulse-detection efficiency for the NuMoon observing mode of
159 LOFAR.

160 3. Filtering

161 Because of limitations in communication bandwidth and processing power at the station
162 level, only 244 of the 512 subbands can be processed online. The data from these subbands
163 will be sent to CEP, and CEP will search these data for signs of a NuMoon pulse. If a pulse
164 is found, CEP will trigger a data-upload. To reduce the occurrence of false triggers, we must
165 select 244 subbands that are free from Narrowband Radio-Frequency Interference (NRFI). In
166 Sec. 3.1 it is shown that this can easily be done by introducing an NRFI mask. It will however
167 be necessary to monitor the NRFI situation so that the NRFI mask can be adjusted if new
168 NRFI lines appear. Broadband Radio-Frequency Interference, also called transient noise in
169 this work, is much harder to eliminate as it may resemble the short pulses we search for. This
170 transient noise is addressed in Sec. 3.4.

171 Once NRFI lines have been excluded, we have some freedom to make a selection of the
172 remaining subbands. Two considerations enter here. One is that the sensitivity for Lunar
173 pulses is highest at the lowest frequencies, as is re-iterated in Sec. 3.2. A second criterion is
174 that the subband selection will affect the structure of the time-domain data that is reconstructed
175 at CEP. In turn, this structure affects how well CEP detects NuMoon pulses.

176 *3.1. Narrowband radio frequency interference mitigation*

177 In Fig. 2 a typical frequency spectrum of a single HBA tile of LOFAR is shown as was
 178 recently measured. Apart from the strong, narrow radio-frequency line at 169.65 MHz [49],
 179 there are a few other narrow lines in the frequency spectrum. These other lines are not always
 180 seen in the spectrum. Nonetheless, they must be filtered out of the NuMoon data, since they
 181 contain an appreciable fraction of the power in the bandwidth when they are present. This
 182 filtering is referred to as NRFI mitigation, where NRFI stands for Radio Frequency Interference
 183 at a well defined frequency.

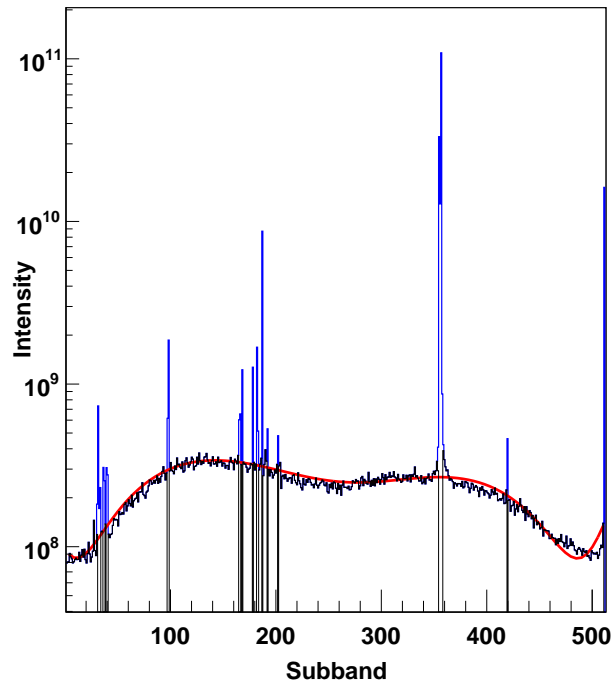


Figure 2: The blue curve shows the intensity (in arbitrary units) per subband, summed over 1 ms for a single HBA tile. The fitted polynomial is shown in red. The NRFI subtracted spectrum is shown in black. Each subband has a width of 195.3125 kHz and the first (last) correspond to 100 MHz (200 MHz). The 354th subband contains the strong 169.65 MHz signal.

184 One possible NRFI mitigation procedure is as follows. First, the frequency spectrum for one
 185 polarization (blue curve in Fig. 2) is summed over one block of data (1 ms) consisting of 200
 186 pages, where each page of $5 \mu\text{s}$ contains 1024 time samples. This summed spectrum is fitted
 187 with a 6th order polynomial (red curve in Fig. 2). The frequency subbands containing a power
 188 exceeding the fit by more than 50% are marked as NRFI lines. For this reason the fit does not
 189 have to be very detailed. The subbands near the edges of the bandwidth are suppressed by
 190 the filters and are for this reason excluded from the analysis. The contents of these subbands
 191 are set to zero, giving the black curve in Fig. 2. This type of NRFI mitigation is known as
 192 masking. NRFI lines are not constant, so the mask must be updated once every few seconds
 193 or so. This procedure was applied in the analysis presented in Ref. [17, 18].

194 For LOFAR, the NRFI mitigation needs to be done online. We thus have to minimize the
 195 extra latency in the data processing on CEP, which implies that online we have to work with

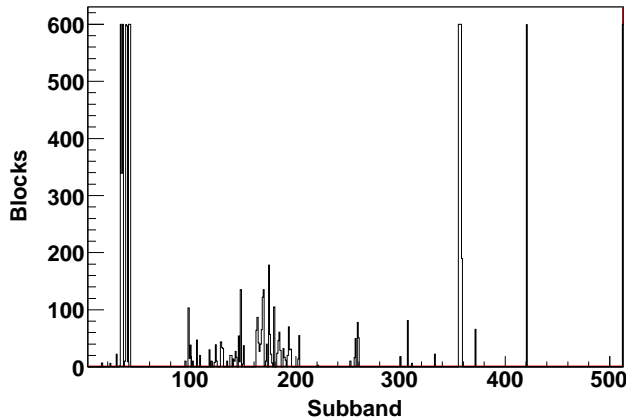


Figure 3: The number of blocks of 1 ms in which a subband is corrupted by NRFI is plotted vs. subband number for 0.6 seconds of single HBA tile data.

196 a pre-defined frequency mask and cannot use the procedure outlined above. For this reason
 197 we have performed an offline check on the HBA data, using a mask that updates regularly.
 198 Fig. 3 shows the number of blocks of data (of 1 ms each) in which a subband is dominated by
 199 NRFI. This is done for all 512 frequency bins (subbands) for 0.6 second of data (600 blocks) of
 200 a single tile as obtained from the TBB. The 169.65 MHz signal appears in every page and the
 201 count for this line reaches the maximum of 600 in the 354th subband. Also the 420th subband
 202 is strongly affected by NRFI. In the first few subbands there are also continual NRFI lines, as
 203 shown in Fig. 3, however, the filter gain is low for these subbands (see Fig. 2). Please note that
 204 the spectrum shown in Fig. 2 is only one of many needed to generate Fig. 3. There is also a
 205 region between the 100th and 200th subband where at times NRFI lines appear. It should be
 206 noted that we have checked the NRFI situation at different hours of the day (at 5 AM, 11 AM,
 207 5 PM and 11 PM) and the worst situation, occurring at 11 in the morning, is given in Fig. 3.

208 Based on the observations presented in Fig. 2 and Fig. 3 we have made an NRFI-mask
 209 excluding subband with central frequencies at 131.64, 133.79, 169.14, 169.53, 169.72, 196.92
 210 and 181.83 MHz. It should be noted that, because the NRFI frequencies depend on the time
 211 of the day, the NRFI mask needs regular updating in the actual observations. The relation
 212 between subband number n and its central frequency is given by $\nu = 100 \text{ MHz} + n d\nu$ with
 213 $d\nu = 195.3125 \text{ kHz}$. In addition we have also excluded the low-gain bands from our analysis
 214 with frequencies below 110 MHz and above 190 MHz.

215 3.2. Optimum window

216 In the design of the optimum trigger condition two aspects need to be considered. The
 217 first is the spreading of the pulse in the time domain due to the partial bandwidth and due
 218 to ionospheric dispersion. The second important aspect is the variation of the sensitivity of
 219 LOFAR over the frequency regime.

220 The effective area of the HBA tiles of LOFAR can be written as [45, 47]

$$A_{\text{eff}} = \min(\lambda^2/3, 1.5625) \text{ m}^2, \quad (1)$$

221 where the change over from a constant to a frequency dependent effective area occurs at a
 222 frequency of 138 MHz. The other important ingredient is the system temperature $T_{\text{sys}} =$

223 $T_{\text{sky}} + T_{\text{inst}}$, where $T_{\text{inst}} \approx 200$ K is the instrumental temperature, and the sky temperature can
 224 be written as

$$T_{\text{sky}} = T_{s0} \left(\frac{\lambda}{1 \text{ m}} \right)^{2.55}, \quad (2)$$

225 where $T_{s0} = 60 \pm 20$ K and λ has units of m. With these two ingredients the system equivalent
 226 flux density (SEFD) for Nyquist sampling can be expressed as

$$S_{\text{sys}} = \frac{2\eta k T_{\text{sys}}}{A_{\text{eff}}}, \quad (3)$$

227 where k is Boltzmann's constant (1.38×10^{-23} J/K) and $\eta \approx 1$ is the system efficiency factor.
 228 The SEFD, tabulated in Table 1, can be regarded as the strength of a signal that, when
 229 coherently summed over all antennas, gives the same induced power as that of the noise.
 230 Recent measurements [46] support the general frequency dependence with an absolute value
 231 that is about 15% higher

Table 1: SEFD for a LOFAR core HBA antenna field consisting of 24 tiles. The last column gives the relative count rate for neutrino detection as function of frequency.

Freq [MHz]	Core [kJy]	C_ν [arb]
120	3.6	1.5
150	2.8	1.0
180	3.2	0.6
210	3.7	0.4

232 The optimum condition for the trigger is that the largest number of Moon pulses will be
 233 detected. For a given frequency ν we have calculated the relative count rate

$$C_\nu = \int dE \Phi(E) P_\nu(E), \quad (4)$$

234 where E is the neutrino energy, $P_\nu(E)$ the chance of detecting a signal at frequency ν from a
 235 neutrino of energy E , and $\Phi(E)$ is the neutrino flux. The latter is often chosen proportional
 236 to E^{-2} [32]. The detection probability is calculated using the procedure discussed in Ref. [16]
 237 including a realistic frequency dependence of the pulse. The threshold for detecting a Lunar
 238 pulse is taken proportional to the SEFD given in Table 1, where the constant of proportionality
 239 cancels in taking ratios.

240 The relative count rates calculated from the SEFD and given in Table 1 show that it is
 241 strongly favorable to include as many of the lower frequencies in the window as possible. Care
 242 should be taken with subbands number 100–200 where there are a large number of intermittent
 243 NRFI lines (see Fig. 3). It should be noted that it is not advantageous to measure at even
 244 lower frequencies than given in the table partly because the smaller effective area of the LBA
 245 fields and partly because the rapid increase of the sky temperature.

246 *3.3. Frequency filter and pulse structure*

247 As mentioned before, due to bandwidth limitations only 244 of the 512 subbands can be sent
 248 to CEP for real-time processing. To make the optimum choice for this selection we have to take
 249 into account the considerations discussed above, i.e. lower frequencies give a larger aperture,
 250 and NRFI-free subbands should be selected that have a gain greater than half of the average.
 251 An additional consideration is that when the bandwidth limited signal is transformed back to
 252 the time domain, a pulse is still narrow in time such that a sensitive trigger can be constructed.
 253 The pulse form will depend on the particularities of the selection of 244 subbands, referred to
 254 as the Frequency-Filter Scheme (FFS)¹. We have analyzed a few different FFSs. For all choices
 255 we have omitted the low-gain as well as the NRFI corrupted subbands.

256 **LoB** One large window at the lowest frequencies.

257 **Log** To give some weight to the higher frequency subbands the selected frequency channels
 258 follow a logarithmic pattern with a greater density at the lower frequencies. Including
 259 higher frequency components may sharpen the signal.

260 **Comb** As an extreme for sharpening the signal structure the frequency channels are selected in
 261 a comb-like structure of groups of 50 subbands which are NRFI-free.

262 **HiB** One large window at the highest frequencies. Even though this choice will not optimize
 263 the aperture, it diminishes the effects of ionospheric dispersion as will be discussed in
 264 later sections.

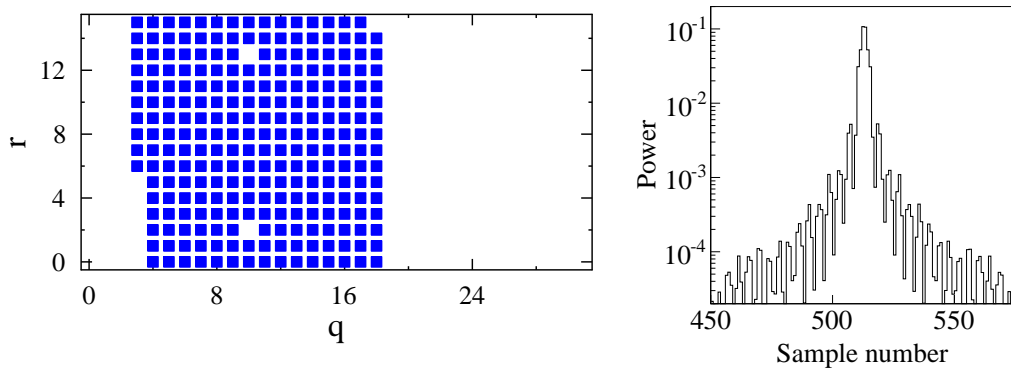


Figure 4: For the LoB-FFS the selected frequencies are shown on the l.h.s., while the r.h.s. shows the response of the filter to a very short bandwidth limited pulse.

265 Each of these FFSs is illustrated in Figures 4–7. The selected frequency window is shown on
 266 the l.h.s., where the subband number is equal to $16q + r$. The r.h.s. displays the corresponding
 267 pulse response in units where the original pulse carries unit power. It is clear that the pulse
 268 response is very different for the various FFSs which will be reflected in the efficiency of recov-
 269 ering it from the noise. The additional effects of ionospheric dispersion will be investigated in
 270 Sec. 5.

¹We used 246 subbands in the simulation, as this used to be the maximum number of bands for the core. The difference will not affect our results.

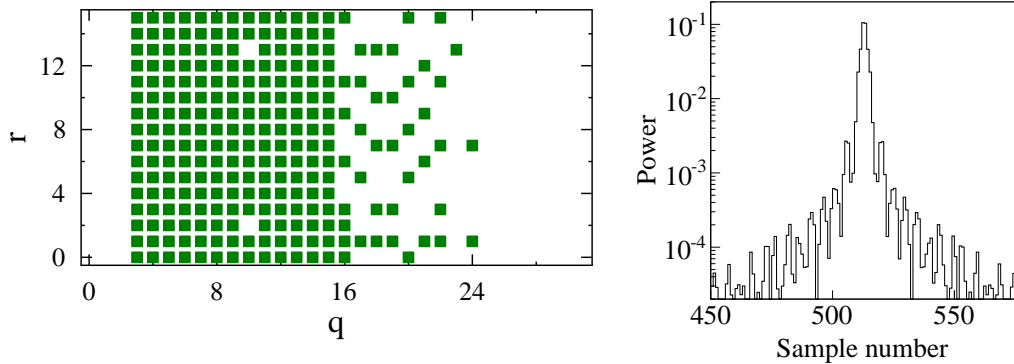


Figure 5: Same as Fig. 4 for the Log-FFS.

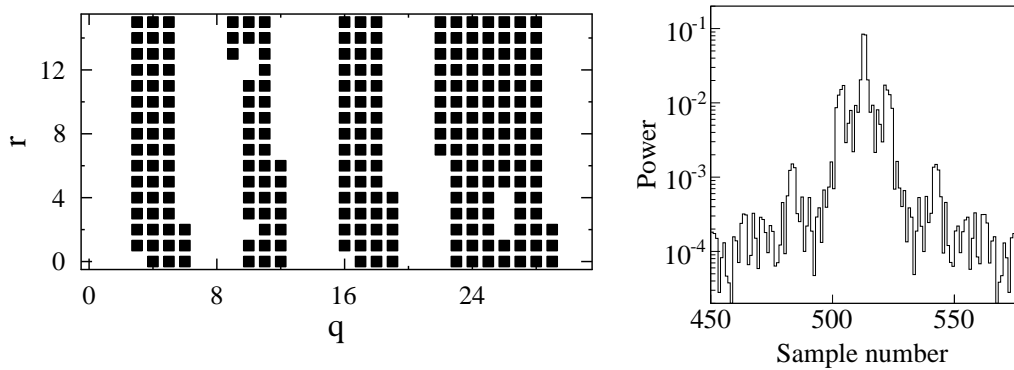


Figure 6: Same as Fig. 4 for the Comb-FFS.

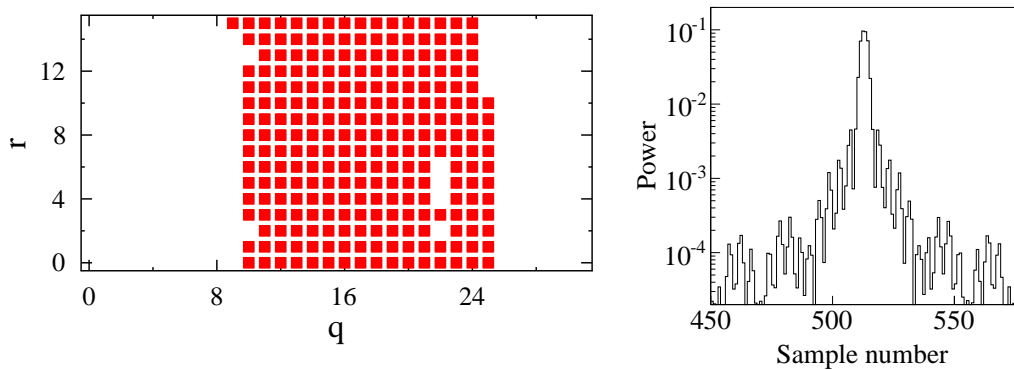


Figure 7: Same as Fig. 4 for the HiB-FFS.

271 *3.4. Noise with different filtering methods*

272 Before adding a pulse to a background (noise) spectrum we investigate the structure of the
 273 data, in particular the extent to which the noise can be regarded as Gaussian. For this we
 274 have processed 1 second raw time-series data from a single HBA tile of LOFAR. These data
 275 contain no NuMoon pulses; it is simply a sample of the noise levels of LOFAR. The data are
 276 passed through the simulated PPF (see Appendix A), after which the NRFI lines in frequency
 277 domain are removed (see Sec. 3.1). The data are transformed back to the time domain by
 278 applying the PPF inversion routine. The resulting amplitude distribution is shown in Fig. 8.

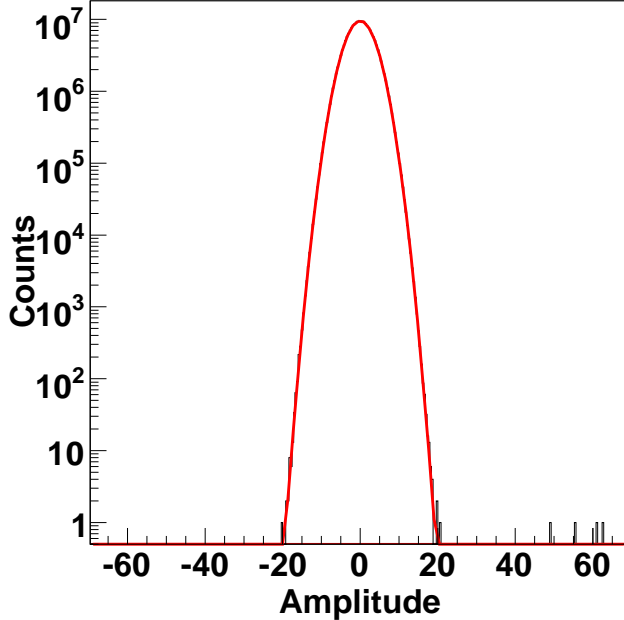


Figure 8: The number of times an amplitude is observed in 1 s of data stream of single HBA tile of LOFAR after NRFI mitigation is plotted vs. amplitude for a unit bin-size. The smooth curve (hardly distinguishable from the histogram) shows a fitted gaussian to the data.

279 The drawn curve shows a Gaussian profile fitted to the data. The χ^2 of the fit is close to
 280 unity showing that the noise closely resembles Gaussian noise. Due to noise transients, the
 281 data shows a small number of large pulses well above the expectation based on the Gaussian
 282 profile. A closer investigation of these large pulses indicates that they are single timing-sample
 283 upsets. On the basis of the experience obtained from observations with WSRT [17, 18] and
 284 preliminary analysis of LOFAR data we expect that most of them diminish in importance when
 285 the signals of a large number of antennas are coherently added and the that remaining ones
 286 can be eliminated by the requirement that they originate from a well-defined spot on the Lunar
 287 surface.

288 On the basis of these results we conclude that for an investigation of the relative merits of
 289 the various FFSs it is sufficient to run simulations where a pulse is added to a Gaussian-noise
 290 spectrum.

291 4. Pulse-search algorithm

292 Central to the trigger algorithm is the pulse-search routine. For this we investigate the
 293 most efficient way to search the data for short, bandwidth-limited pulses of the type that may
 294 result from a cosmic ray or neutrino hitting the Moon. The basic search algorithm consists
 295 of measuring the power of an incoming signal over a certain amount of time. This can be
 296 visualized as a window of time sliding over the data. We must identify both an optimum FFS
 297 and an optimum size N for the window sliding over the data. This is done through simulations
 298 where we add pulses of different magnitudes to a spectrum of simulated pure Gaussian noise.
 299 The magnitude of these pulses is measured in terms of the average noise power, σ^2 . A pulse is

300 added at a random time-position in every third page of a set of 3 pages. Each page contains
 301 1024 time-samples.

302 Our aim is to design triggering criteria such that a large percentage of pulses from the
 303 Moon will be processed while suppressing random noise triggers. For definiteness we have
 304 set the random-trigger level at about once every minute. In realistic situations one is limited
 305 by the system's dead-time (estimated at about 5 seconds per event) and storage capabilities.
 306 The deadtime is inherent to the way LOFAR manages data: LOFAR's TBBs and station
 307 processors use the same data buses to communicate with CEP. Triggering causes the TBBs
 308 to dump data to CEP, and while this dumping is in progress no new data can be recorded at
 309 the TBBs. While not long, this deadtime will cut into the efficiency of NuMoon if triggering
 310 occurs too frequently. As mentioned earlier, the use of anti-coincidence criteria will reduce the
 311 number of triggers caused by transient noise. In this work we apply the pulse-search algorithm
 312 separately to each polarization. In the calculation of the sensitivities to pulses from UHE
 313 neutrinos, this is accounted for by assuming that the pulse power is distributed 50-50 over the
 314 two polarizations. This will constitute an underestimate of the efficiency since adding the two
 315 polarizations incoherently will increase the signal over noise ratio.

316 *4.1. Power of N consecutive time samples (P_N)*

317 To analyze the time series we retrieve the power from a sliding window of size N bins of
 318 5 ns,

$$P_N(i) = \frac{1}{\sigma^2} \sum_{n=1}^N v_{(i+n)}^2 . \quad (5)$$

319 where v_i is the voltage for the i^{th} time sample. As mentioned before, the noise power σ^2 is
 320 defined as the average power per time sample for a full bandwidth spectrum, after subtracting
 321 the sharp-frequency RFI lines.

322 For every page of 1024 time samples, the maximum power in the window is defined as

$$P_N^{\text{m}} = \max_i P_N(i) , \quad (6)$$

323 Depending on the value of this maximum, a trigger flag will be set. In order to choose a
 324 threshold for P_N^{m} we first analyze the structure of the noise which depends on the FFS that is
 325 used.

326 *4.2. Accidental noise pulses & threshold determination*

327 Sometimes noise will cause a trigger-flag to be set. This is referred to as an accidental
 328 trigger. In order to predict the rate at which accidental triggers occur, we have analyzed the
 329 noise with the sliding window method. The distribution of P_N^{m} values is determined for a sample
 330 of 1 second filled with Gaussian noise. This analysis is repeated for all FFSs and for a range
 331 of window sizes N . The general features of the distribution are independent of the particular
 332 FFS or the value of N that has been used. As an example, in Fig. 9 the distribution of P_N^{m} is
 333 plotted for $N = 7$ and the LoB-FFS.

334 In the analysis we aim to set a threshold value for P_N^{m} which will result in a certain maximal
 335 accidental trigger rate. For the present analysis, we have set the maximal accidental trigger
 336 rate at once per minute. For each P_N^{m} distribution, we have determined the threshold value P_N^{t}

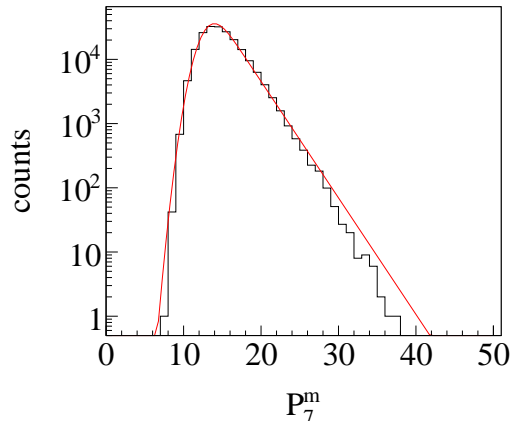


Figure 9: Plotted are the number of occurrences of a P_N^m value per unit bin size for 1 second of Gaussian noise filtered with the LoB-FFS for $N = 7$. The drawn, red, curve shows the fit to the spectrum using Eq. (8).

337 where we expect to find a value $P_N^m > P_N^t$ only once per minute. The value of the threshold
 338 is determined by fitting a particular function $F(x)$ to the distribution of $P_N^m = x$. For a large
 339 value the distribution should follow that of a χ^2 distribution with k degrees of freedom,

$$P(x, k) \propto x^{k/2-1} e^{-x/2} . \quad (7)$$

340 To a good approximation the number of independent degrees of freedom in the distribution is
 341 given by $k = N/2$ since, due to the FFS, the signal is oversampled by almost a factor two. For
 342 simplicity we have chosen to fit the spectrum by a convolution of a Gaussian and an exponential
 343 that is cut off at the lower end,

$$F(x) = B \int_{p_{co}}^{\infty} e^{-(x-x')^2/\sigma^2} e^{ax'} dx' , \quad (8)$$

344 with fitting parameters B (a normalization factor), σ (the width of the Gaussian), p_{co} (the x -
 345 value where the exponential is cut off) and a (the slope of the exponential). $F(x)$ is integrated
 346 to determine the value of P_N^t which will correspond to the desired accidental trigger rate. As
 347 is clear from Fig. 9, the distribution is overestimated for large values of P_N^m . Working with the
 348 fitted curve thus gives rise to a higher value for P_N^t than would be necessary on the basis of
 349 pure Gaussian noise.

350 The thus determined values of P_N^t for the various FFSs and window-sizes are given in
 351 Fig. 10. With increasing window-size N one expects the threshold P_N^t to increase, since the
 352 time-average power in a window is proportional to the size of the window. This explains the
 353 rising trend one sees in the determined values of P_N^t for each FFS. Note that the various FFSs
 354 introduce correlations in the noise-spectra, which are reflected in the differences one sees in
 355 their P_N^t values.

356 4.3. Pulse amplitude distribution

357 As was shown in Sec. 3.3, the selected FFS strongly affects the measured shape of the
 358 pulse in time, and in general the pulse will broaden. With increasing size (N) of the sliding

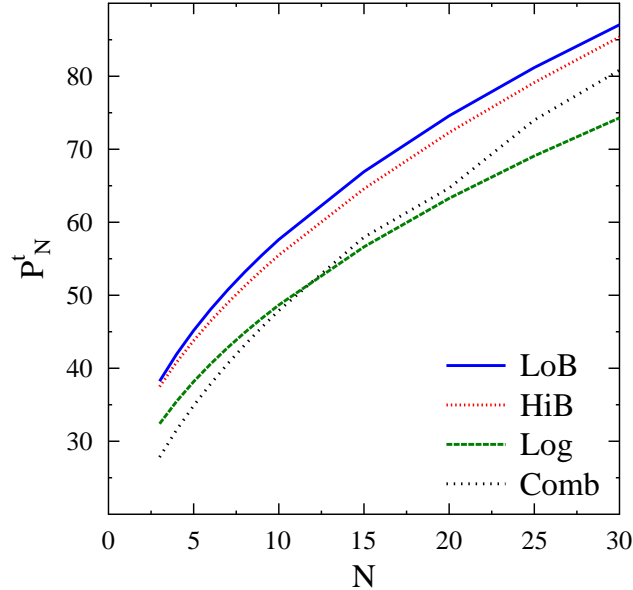


Figure 10: The determined threshold values P_N^t , corresponding to 1 accidental count per minute, as function of N for the different FFS under consideration.

359 window, a larger fraction of the broadened pulse will be recovered. However, increasing the
 360 size of the sliding window will also capture more noise power (see Fig. 10). At a certain point,
 361 this captured noise power will no longer balance the increase in captured pulse power causing
 362 a worsening of the signal-to-background ratio. As a first step towards finding the optimum
 363 size of the window, we investigate how well the original power of the pulse is recovered by the
 364 sliding-window procedure.

365 We start with a very short, delta-function like in time, pulse of unit power (when integrated
 366 over the full bandwidth of the HBA subbands, before applying and filters) placed at a random
 367 position in a page. The pulse is processed as described earlier: The FFS is applied after a
 368 16 tap PPF, and then the signal is converted back into the time domain by applying a full
 369 PPF-inversion (PPF^{-1}). The maximum power found in a window of length N is taken to be
 370 the recovered power of the pulse. This recovered power is compared to the original power of
 371 the pulse (here, original power = 1). The recovered power depends on the structure of the
 372 recovered pulse, which in turn depends on the phase of the sampling-cycle at the time the pulse
 373 arrives. (One full sampling-cycle is equal to one time-sample.) To account for the fact that a
 374 pulse may arrive at any phase of the sampling-cycle, the analysis is repeated 1000 times with
 375 the pulse arriving at various phases of the sampling-cycle. The average value of the recovered
 376 power, \bar{P}_N^m , is shown as a percentage of the power of the input pulse in Fig. 11. This procedure
 377 was applied for every value of N between 3 and 50, and for each of the FFSs. This part of the
 378 analysis has been done without adding noise to the spectrum.

379 With increasing window length N , an increasing fraction of the power of the input pulse
 380 is recovered. The retrieved power saturates at about 50% due to the bandwidth of the FFSs.
 381 For small values of N the Comb-FFS performs considerably worse than the other FFSs. This
 382 can be understood from Fig. 6 where it is shown that the peak of the power distribution is
 383 considerably wider than that for the other FFSs. The lower saturation value for the Log-FFS

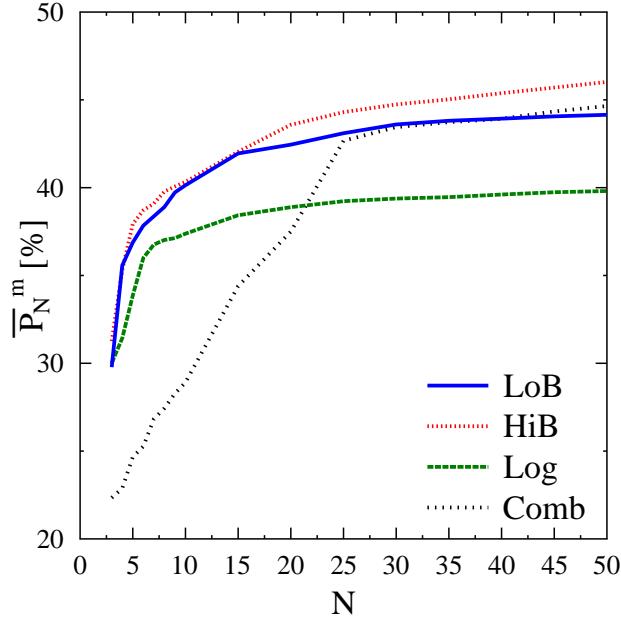


Figure 11: Percentage of retrieved power for pulses with random phases for the different FFSs. This analysis is performed without a noise background.

384 is due to the fact that in this FFS there is considerably more power in channels more than 100
 385 time samples removed from the peak (outside the range shown in figures (4 ··· 7)). As is shown
 386 in Sec. 4.2 the noise will continue to increase with N . We expect that there is an optimum for
 387 N . To search for this optimum N , we repeat the previous analysis with noise included.

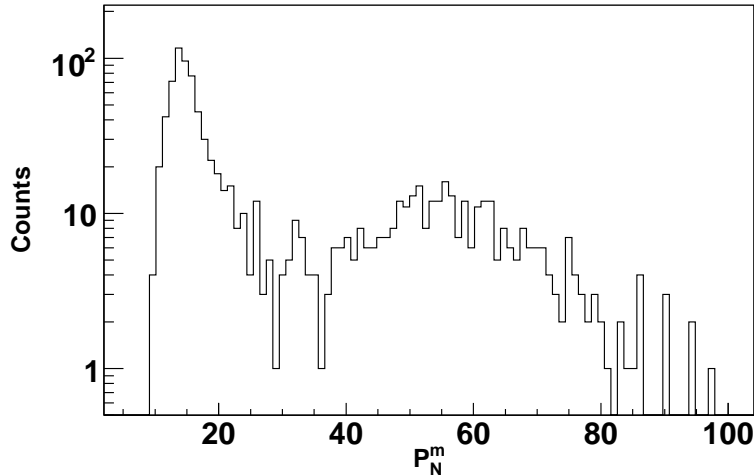


Figure 12: Histogram of the number of occurrences of a P_N^m value per unit bin size when a pulse, with power $144\sigma^2$, is added to a noisy background for every third page and filtered with the Comb-FFS, using $N = 15$.

388 When including noise in the analysis the picture becomes more complicated since the pulse
 389 and the noise will interfere. To study this case we have analyzed 1000 pages of 1024 time-

390 samples each containing Gaussian noise with a power of σ^2 per time sample. To each third
 391 page a pulse with a predetermined power is added with a random phase at a random position.
 392 The time traces are run through the complete simulated NuMoon pipeline, including the FFS,
 393 and for each page the value of P_N^m is determined. As an example, the spectrum of P_N^m values
 394 for $N = 15$ is plotted in Fig. 12 for a pulse with power $144 \sigma^2$ using the Comb-FFS. At lower
 395 values of the power, the noise is following the spectrum shown in Fig. 9, since two-third of
 396 the analyzed pages contain exclusively Gaussian noise. Centered around a value of about 60 a
 397 broad bump shows. This is due to those pages where a pulse was added.

398 It is instructive to develop a feeling for the numbers. When a pulse of power $A^2 \times \sigma^2$ is
 399 added to noise this will give a broad structure in the spectrum of P_N^m values with the centroid at
 400 $\bar{P}_N^m = A^2 \times E + N/2$ where $E \approx 0.4$ is the efficiency of power reconstruction (see Fig. 11). Since
 401 the FFS approximately halves the bandwidth, a window of length N contains a noise power of
 402 $\sigma^2 N/2$. Due to interference with the noise the structure extents from $P_N^m = (A - 1)^2 \times E + N/2$
 403 till $P_N^m = (A + 1)^2 \times E + N/2$ and has thus a width of $\Delta P_N^m = 4A \times E$. The value of the
 404 threshold for which about 80% of the added pulses is recovered thus can be approximated as

$$P^t \approx (S_{80} - 1)^2 \times E + N/2 \quad (9)$$

405 or inverted as

$$S_{80} \approx \sqrt{P^t/E} + 1, \quad (10)$$

406 essentially independent of window length N . The polarization degrees of freedom have not
 407 been considered. For $N = 15$, $A = 12$ and $E = 0.35$ one thus expects on average a value
 408 $\bar{P}_N^m = 144 \times 0.35 + N/2 = 58$, which agrees well with the result shown in Fig. 12. Also, the
 409 predicted width of the structure $\Delta P_N^m = 4A \times 0.35 = 17$, which agrees with the figure. On the
 410 basis of these consideration, for a 1 min observation the S_{80} value for $P_N^t = 58$ is thus expected
 411 to be $S_{80}^{1m} = \sqrt{58/0.35} + 1 = 13.8$, which is close to the value given in Fig. 14 for the Comb-FFS
 412 with $N = 15$.

413 For the data analysis it is important to know what percentage of added pulses of a certain
 414 magnitude produces a value for P_N^m that exceeds the trigger threshold P_N^t , which was discussed
 415 in Sec. 4.2. This number, the detection efficiency, is discussed in the following section.

416 4.4. Detection efficiency

417 To quantitatively compare the different FFSs and window-sizes, we have added pulses to
 418 Gaussian noise at random positions in every third data page of 1024 time-samples each, as
 419 discussed in the previous section. The data are run through the complete signal processing chain
 420 (see Fig. 1) including the PPF transformation, beam forming, selecting NRFI-free frequencies
 421 and the back transformation to time sampled spectra. A trigger-flag is set when the value of
 422 P_N^m for one data page exceeds the threshold value P_N^t (discussed in Sec. 4.2). The detection
 423 efficiency (DE) for a particular combination of FFS and N is defined as the fraction of added
 424 pulses that generate a trigger signal.

425 In Fig. 13 the DE is compared for the various FFSs. The DE is given as a function of
 426 the strength of the added pulses. Similar plots are made for a range of sizes N of the sliding
 427 window. For a good operation of the NuMoon trigger scheme we demand a DE of 80% or
 428 better. For each combination of FFS and N , we can determine a pulse-amplitude S , in units of
 429 σ , for which the detection efficiency is 80% ($S_{80}(N)$). For each FFS the value of S_{80} is plotted
 430 as function of N in Fig. 14.

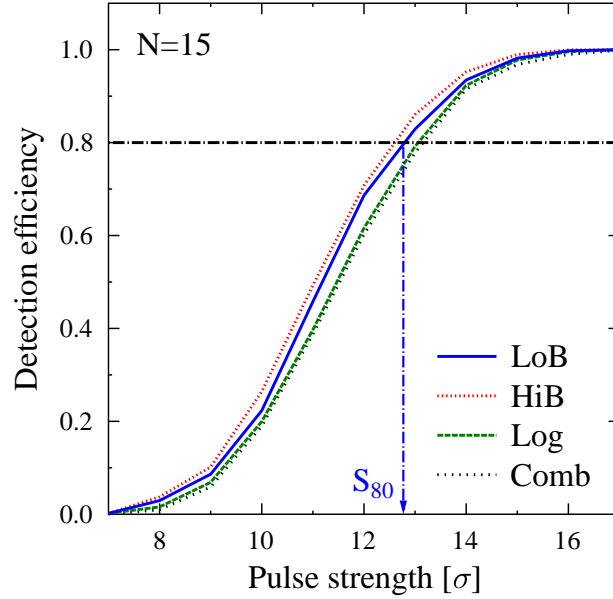


Figure 13: Detection efficiency is analyzed for the different FFSs with $N=15$ as a function of the power of the pulse. The 80% recovery limit is indicated by the dash-dotted curve.

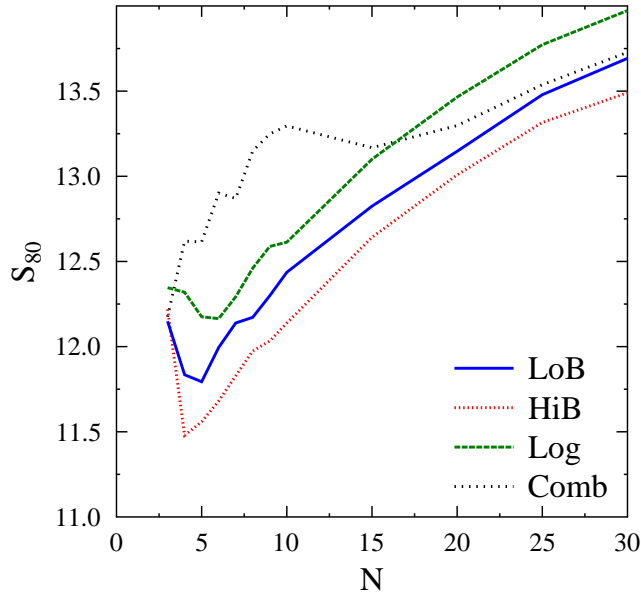


Figure 14: The pulse strength is given for which the DE exceeds 80% (S_{80}) as function of the window size N for the different FFS under consideration.

431 For most of the FFSs, Fig. 14 shows a trend that we can easily explain based on the previous
 432 discussions. With increasing window length the noise power in the window increases, which
 433 necessitates an increase in threshold value, P_N^t , to reach a constant accidental count rate (see
 434 Fig. 10). The value of P_N^t increases faster than the recovered pulse power, shown in Fig. 11,
 435 resulting in increasing values for S_{80} which are seen in Fig. 14 at large values of N . For

436 all FFSs, except for the Comb-FFS, the initial decrease in S_{80} for small values of N is thus
 437 clearly due to the strong increase of pulse power. For the Comb-FFS the recovered pulse power
 438 increases step-wise because of the satellite structure of the pulse induced by this particular FFS
 439 (see Fig. 6) and the drop in S_{80} is seen only around $N = 15$ where the first satellite starts to
 440 fall inside the sampling window.

441 5. Ionospheric dispersion

442 Since we are looking for short radio pulses coming from the Moon, we need to correct
 443 for the ionospheric dispersion of the pulse. Ionospheric dispersion causes the pulse to arrive
 444 later at lower frequencies, effectively causing the pulse to broaden in time. The dispersion
 445 is proportional to the total column density of electrons, the Total Electron Content (TEC).
 446 TEC is a meteorological phenomenon, and it changes continuously, but most strongly during
 447 sunrise and sunset. Relevant to the present discussion is the slanted TEC (STEC) which is the
 448 TEC value in a slanted column along the observer's line of sight. STEC and TEC are usually
 449 expressed in terms of TEC units (TECU) where $1 \text{ TECU} = 10^{16} \text{ electrons/m}^2$. The phase shift
 450 at a particular frequency is given by

$$\phi(\nu) \approx 2\pi \frac{1.34 \cdot 10^9 \text{ STEC}}{\nu} . \quad (11)$$

451 In order to correct for dispersion, we must have a good measure of the STEC which caused the
 452 dispersion. An estimate of the STEC value is available from GPS observations with a precision
 453 of about $\pm 1 \text{ TECU}$. For LOFAR, it is likely that the STEC value can be determined even more
 454 precisely using images from point sources or Faraday rotation. Note that CEP will only use
 455 data from the core stations to determine the trigger. This means that only the STEC at these
 456 stations is relevant to triggering. The core stations cover an area of $2 \times 2 \text{ km}^2$, not a large area
 457 as far as ionospheric phenomena are concerned. This means that local variations of TEC can
 458 be ignored. A single STEC value will be sufficient for de-dispersion of all the core LOFAR
 459 stations (see Fig. 1).

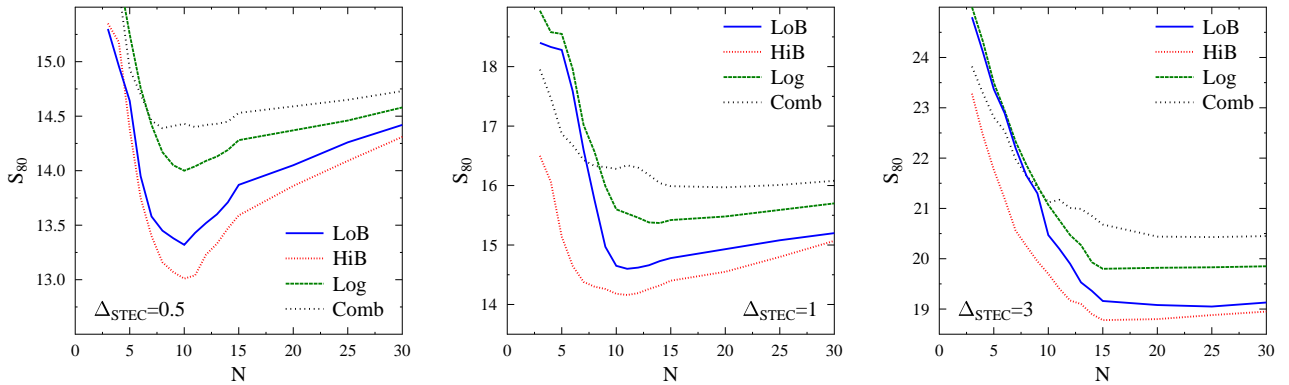


Figure 15: Same as Fig. 14 now including a gaussian spread in the STEC error with a standard deviation increasing from left to right, taking the values of $\Delta_{\text{STEC}} = 0.5, 1.0, \text{ and } 3.0 \text{ TECU}$ respectively.

460 To determine the accuracy to which the STEC needs to be known to perform the proposed
461 Lunar measurements, we have repeated the previous analysis taking a particular STEC value,
462 termed simTEC (=8 TECU in this case), to disperse the pulse that is added to the data. In the
463 analysis step the pulse is recovered taking different values of the STEC to simulate an error.
464 The difference between the two STEC values is taken according to a Gaussian distribution
465 with width Δ_{STEC} . The results of these calculations are shown in Fig. 15 for different values
466 of Δ_{STEC} . These figures should be compared with the results displayed in Fig. 14. One notices
467 that some clear trends in the plots. The S_{80} values at small values of N rapidly increase.
468 This is can easily be understood from the fact that the uncorrected part of the dispersion
469 of the signal introduces a lengthening of the pulse for an increasing number of time samples
470 reducing the recovered power in a small time window. The same argument also explains that
471 the optimum value for N increases towards larger values with increasing Δ_{STEC} . As a result
472 the optimum value for the window size increases towards larger values at increasing values of
473 the pulse strength that can be recovered with a good efficiency, S_{80} .

474 On the basis of these simulation one thus concludes that for the real observations one should
475 strive to determine the STEC value within an accuracy of $\Delta_{\text{STEC}}=0.5$ TECU. In the simulations
476 to determine the sensitivity for detecting UHE neutrinos we will assume $\Delta_{\text{STEC}} = 1.0$ TECU
477 and take $N = 15$ to be on the conservative side.

478 6. Beaming

479 In this section the pulse-detection algorithm is integrated in a realistic antenna configuration
480 where we consider the aspects of beaming. A beam profile is calculated which differs from
481 the usual profiles in the sense that this profile reflects the detection efficiency of broad-band
482 transients. In the calculations the profiles of the tile beams have not been folded in.

483 Fig. 16 shows the layout of the LOFAR core stations. The fields of HBA tiles for every
484 station are shown by yellow circles. Each field represents a group of 24 HBA tiles. The
485 synthesis of beams using all core stations is required to reach a high sensitivity.

486 Beam widths (FWHM) in the zenith and azimuth angles of tied array beams are indicated
487 for various positions of the Moon in Table 2 for the LoB-FFS. The azimuth angle variation is
488 taken from 120° to 240° (where $\phi = 0^\circ$ is north and $\phi = 90^\circ$ is west) to match the moonrise and
489 moonset directions. The values given in the table can easily be understood from the fact that
490 at $\phi \approx 120^\circ$ the station layout Fig. 16 gives the smallest projected baseline while the largest
491 baseline is seen at $\phi \approx 210^\circ$. The azimuth beamwidth $\Delta\phi$ should thus be largest at $\phi = 120^\circ$
492 and smallest at $\phi = 210^\circ$ as shown by the numbers in the table. Simple geometry shows that
493 $\Delta\phi$ should be independent of zenith angle. Furthermore from geometry one deduces that the
494 beamwidth in zenith angle at (θ, ϕ) equals $\Delta\phi(\theta, \phi - 90^\circ)/\cos\theta$.

495 We will cover the whole Lunar surface with several beams that overlap at the FWHM angle.
496 From the beamwidth given in Table 2 it can be calculated that thus 48 beams are necessary
497 to cover the whole visible Lunar surface (an angular size of half a degree) if it were at Zenith
498 (which it never is). At finite zenith angle θ the angular area of the coherent beams increases
499 and fewer beams, $48 \times \cos\theta$, independent of azimuth angle, are necessary to cover the area of
500 the Moon.

501 The observed beam widths are frequency dependent. For the HiB-FFS, where the wave-
502 lengths are shorter, the widths are more narrow and one finds $\Delta\phi = 0.062^\circ$ and 0.056° as

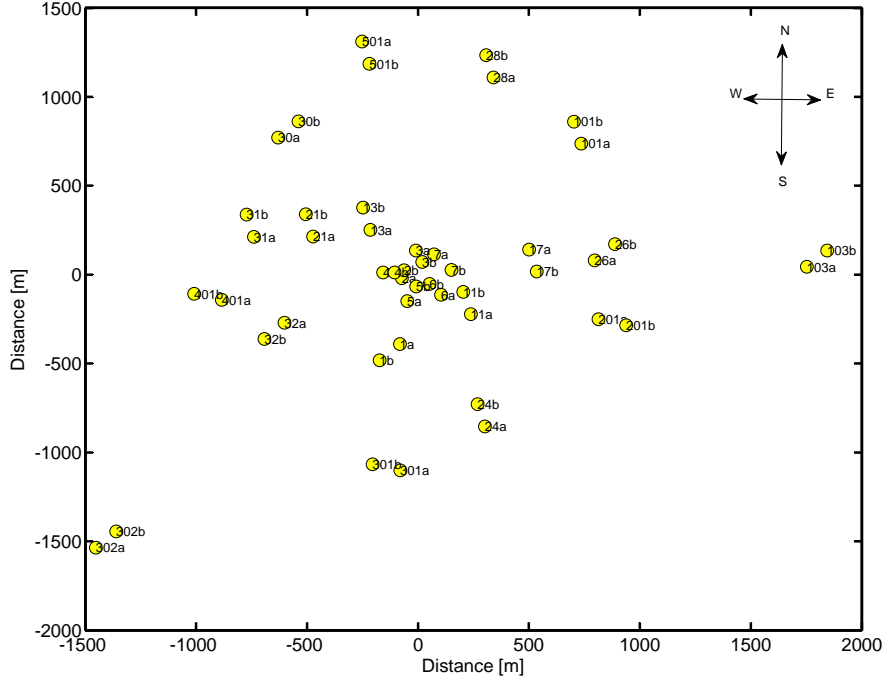


Figure 16: Layout of the HBA fields of the LOFAR core. Each station consists of two fields.

Table 2: Table showing beam widths of LOFAR tied array beam for various position of Moon in the sky, defined by zenith (θ) and azimuth (ϕ) angles in degrees. Simulation are done for the LoB-FFS using all 24 LOFAR core stations. Beam widths are given as Δ_θ , Δ_ϕ .

ϕ	120	150	180	210	240
θ					
15	0.07 0.0756	0.072 0.071	0.076 0.069	0.078 0.068	0.07 0.069
30	0.078 0.075	0.08 0.071	0.086 0.069	0.086 0.068	0.082 0.069
45	0.96 0.075	0.098 0.071	0.104 0.069	0.106 0.068	0.11 0.0693
60	0.139 0.077	0.137 0.071	0.148 0.069	0.15 0.067	0.142 0.069
75	0.264 0.075	0.268 0.072	0.288 0.069	0.292 0.068	0.276 0.069

503 maximum and minimum at $\phi = 120^\circ$ and 210° respectively.

504 An important ingredient of the trigger software is the implementation of an anti-coincidence
505 requirement that will suppress a large fraction of the transient noise. For this it is necessary to
506 investigate the magnitude of the side-lobes for the pulse-response. We have run simulations to
507 model the response to different source directions for the LOFAR core configuration. A pulse

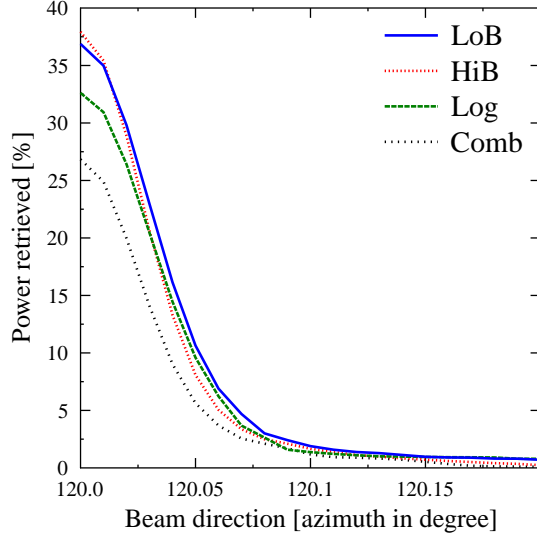


Figure 17: Detection efficiency along azimuth angle ϕ for pulses de-dispersed with no STEC error when the source of the pulse is assumed to be at $(\theta = 60^\circ, \phi = 120^\circ)$.

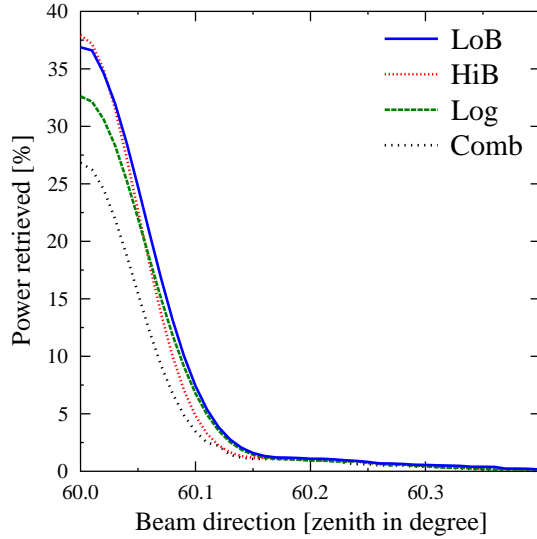


Figure 18: Same as Fig. 17, but for the detection efficiency along zenith angle θ .

508 is added to the time traces of the different core stations as arriving from a certain direction,
 509 $(\theta = 60^\circ, \phi = 120^\circ)$. In the reconstruction the signals are added with phases corresponding
 510 to a slightly different viewing direction. We have not included noise in this simulation as it is
 511 not essential. The full trigger pipeline was simulated. The results for P_N^m using $N = 15$ for the
 512 different FFSs are shown in Fig. 17 and Fig. 18. From these figures it is seen that the sidelobes
 513 are strongly suppressed due to the (almost) random relative positions of the core stations.

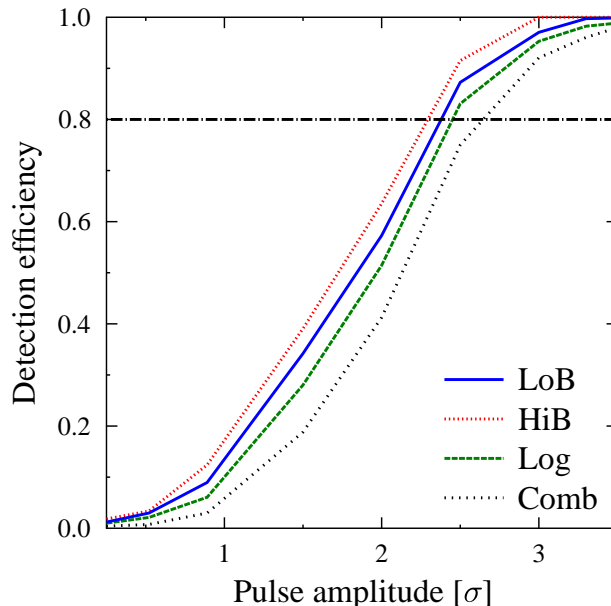


Figure 19: Shown is the detection efficiency for the optimum setting, $N = 15$, using the LOFAR core configuration and averaging over the full-width at half maximum of the beam.

514 7. Energy limit of ultra high energy particle

515 The detection efficiency is investigated for the various filter schemes for the LOFAR core.
 516 Pulses are added to a un-correlated Gaussian background and are dispersed using Gaussian
 517 distributed values around the mean STEC value that is corrected for in the analysis, with a
 518 standard deviation of 1 TECU. The simulations are done for 1000 added pulses. The detection
 519 efficiency for the optimal settings for the window length, $N = 15$, is shown in Fig. 19. This
 520 calculation includes the effects of coherent addition of the 24 stations in the core that are
 521 already deployed where the source is spread over an angular range corresponding to the size of
 522 the beam.

523 The limit for the trigger rate we want to consider is about once every minute. This gives,
 524 using Fig. 19, Table 1, and including a factor $\sqrt{2}$ to account for a linearly polarized signal, an
 525 80% sensitivity for pulses with an intensity in excess of 26 kJy.

526 In calculating the sensitivity of the LOFAR measurements to pulses coming from the Moon
 527 one should realize that the final sensitivity reached in an off-line processing of the data cannot
 528 be larger than the trigger level that has been set. Any pulses with lower strength will not
 529 set the trigger flag and are thus lost for later processing. The limit considered for this work
 530 will be based on a single pulse for the duration of the observations, a few days. In the actual
 531 observations one may consider the number of excess counts over a statistical noise distribution,
 532 however, this requires a perfect understanding of the transient noise which is the subject of a
 533 future work. The highest sensitivity is reached when the post processing is performed using
 534 the full bandwidth information stored on the TBBs while the trigger signal is obtained using
 535 the LoB-FFS.

536 The sensitivity that can be reached in post processing is determined by the accidental rate
 537 for the full LOFAR. A safe limit can be set if the accidental rate vanishes for the duration of

538 the complete observation. Setting this —relatively arbitrarily— to one month we arrive at a
 539 threshold for accidental detection which is increased by a factor of less than 1.5 (using Eq. (7))
 540 as compared to that for one accidental detection per minute (the trigger threshold). The full
 541 LOFAR will have a collecting area that is double that of the core, and we will be able to use
 542 the full bandwidth giving a factor 4 increase in the signal over noise ratio. The 80% sensitivity
 543 level for pulses thus lies at a much lower value than the trigger value of 26 kJy.

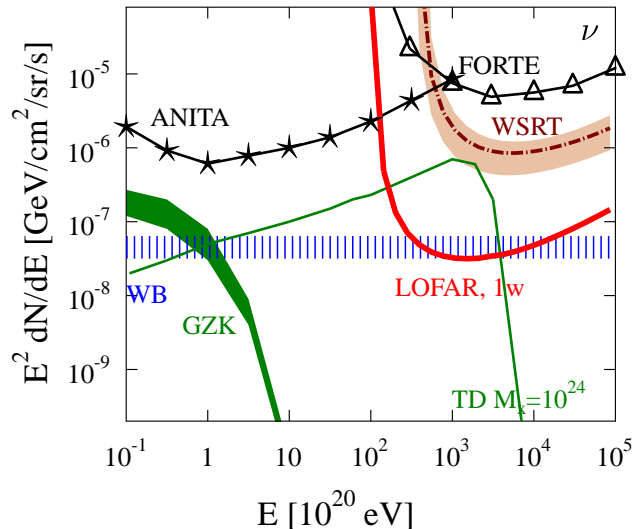


Figure 20: Neutrino flux limits for LOFAR, see discussion in the text.

544 From these considerations it is clear that the determining factor for the observations is set by
 545 the trigger threshold. In Fig. 20 the sensitivity on the neutrino flux for LOFAR is given, based
 546 on the pulse-detection thresholds indicated above. The obtained limit is getting sensitive to
 547 the Waxman-Bahcall flux prediction [32] based on a polynomial extrapolation of the measured
 548 cosmic-ray flux and of the order of 40 counts are expected if the predictions of a top-down
 549 model [33] for exotic particles of mass $M_X = 10^{24}$ eV would be correct. The previous limits
 550 in the UHE region have been set by the ANITA [6] and FORTE [7] experiments. The GZK
 551 neutrino flux indicated in the figure is obtained from the work of ref. [34].

552 The detection threshold for the LOFAR observations is more than an order of magnitude
 553 lower than the 240 kJy for the observations with the WSRT [18]. Since the strength of the pulse
 554 generated by the neutrinos depends quadratically on the energy, the LOFAR observations are
 555 sensitive to neutrinos with much smaller energies, as can be seen from Fig. 20. The increased
 556 sensitivity, combined with the longer observation time makes the observations sensitive to
 557 considerably lower neutrino fluxes.

558 Short radio pulses emitted from the lunar regolith can also be used to detect UHE cosmic
 559 rays. The main differences between the interactions of cosmic-rays and neutrinos in the regolith
 560 is that in cosmic rays all the energy is converted into a particle shower while this is only of the
 561 order of 20% for neutrinos. Another important difference is that while neutrino showers develop
 562 deep inside the regolith, cosmic ray showers develop very close to the Lunar surface. Recently it
 563 has been shown that showers close to vacuum-medium boundary emit electromagnetic radiation
 564 to the same extent as would be obtained by using plane-wave refraction of the waves waves

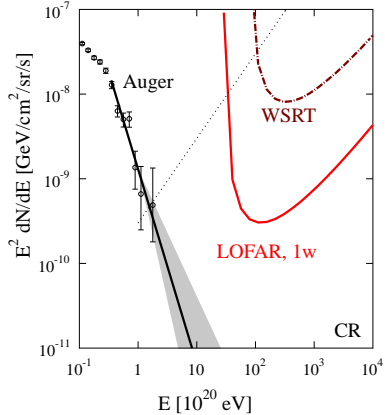


Figure 21: The limit for the cosmic-ray flux as can be determined by LOFAR in one week observation time is compared to the flux determined by the Pierre Auger Observatory [51] (data points with error bars) and a simple polynomial expansion (black line, see text). Also the prospective flux sensitivities are indicated that can be obtained with LOFAR. Shown is also the cosmic-ray flux limit from WSRT observations [18, 50].

565 through the surface [50]. As shown in Fig. 21 this allows for a tightening of the flux limits at
 566 the highest energies, well below the model-independent limits extracted from the data obtained
 567 at the Pierre Auger Observatory [51].

568 8. Summary and conclusions

569 As an essential part of the project to determine the flux of UHE particles through their
 570 impacts on the Lunar surface, we have investigated the most efficient method to detect the radio
 571 pulse, emitted by the impact, in a noisy background. Since the data processing is performed
 572 in real time the calculational latency of the method must be small. To be able to handle the
 573 enormous data rate generated by LOFAR we propose a procedure that consists of two separate
 574 stages. The first stage generates a trigger signal based on limited information available from
 575 the core stations. The trigger causes the complete, full bandwidth, signal from the core as well
 576 as the remote stations to be written to a mass storage system for later processing. In a second
 577 processing stage the stored data will be searched for Moon pulses. At this stage full bandwidth
 578 and the maximum collecting area are available for analysis and thus the ultimate sensitivity
 579 can be reached for pulse detection. This leaves the construction of the trigger signal as the
 580 defining bottleneck in the system.

581 To limit the latency in constructing the trigger we have restricted ourselves to procedures
 582 where the power in a time window is compared to a threshold value. Of particular importance
 583 in determining the window size is the selection of the frequencies used in the construction of
 584 the trigger, as only half the bandwidth can be processed. Another important consideration
 585 is the accuracy with which the signal can be corrected for the dispersion caused by the free
 586 electrons in the upper ionosphere. These factors are taken into account in a simulation and
 587 optimal trigger conditions are determined. On the basis of these optimal settings the sensitivity
 588 of observations to Lunar pulses is determined which translate into flux limits. This shows that
 589 observations with LOFAR, in the frequency range of 100–200 MHz are an order of magnitude
 590 more sensitive than previous observations in this frequency range looking for Lunar pulses.

591 9. Acknowledgements

592 This work was performed as part of the research programs of the Stichting voor Funda-
 593 menteel Onderzoek der Materie (FOM), with financial support from the Nederlandse Organ-

594 isatie voor Wetenschappelijk Onderzoek (NWO), and an advanced grant (Falcke) of the Euro-
595 pean Research Council.

596 Appendix A. The polyphase filter and inversion

597 The fast fourier transform is a very efficient method for transforming the data between
598 the frequency and time domains. However, the resolution in frequency is limited. Without
599 the application of a windowing function (such as a Hamming filter), this causes considerable
600 leakage of signal between neighboring channels in the frequency domain. On the other hand,
601 if a windowing function is applied, considerable intensity is lost. One way to overcome this
602 problem is to work with overlapping the sections of the data incorporated as a polyphase filter
603 bank. The PPF banks are implemented on FPGAs (Field Programmable Gate Arrays) at the
604 LOFAR stations (see Fig. 1).

605 The PPF bank is a combination of a parallel structure of M ($M = 1024$ for the present
606 implementation) sub-filters followed by an FFT stage [44]. Each sub-filter is a Finite Impulse
607 Response (FIR) filter (like the main filter) that filters with $K = 16$ taps (or filter coefficients).
608 The total filter-structure can be represented as a matrix with M rows and K columns where
609 each sub-filter is fed with input data M time samples apart. The weighted average of K input
610 time samples will be summed and fed into the M point FFT.

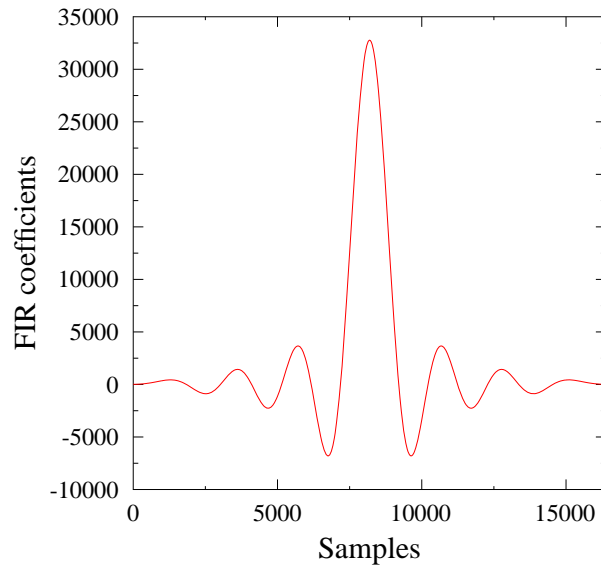


Figure A.22: Impulse response of the implemented FIR filter.

611 The impulse-response of LOFAR's FIR filters is similar to a sinc-function, which inherits
612 the linear-phase of each subband [44]. The implemented impulse-response with all $M \times K$
613 sub-filters is shown in Fig. A.22.

614 The advantage of using the PPF can be seen from the frequency spectrum of the HBAs of
615 LOFAR (Fig. A.23) where there is a strong NRFI at 169.65 MHz. The spectrum on the r.h.s. of
616 Fig. A.23 is obtained by performing an FFT transform on a block of 1024 time samples. This
617 shows that using a PPF is a very efficient way to suppress aliasing of NRFI lines to adjacent
618 subbands which is important for efficient NRFI mitigation, as discussed in Sec. 3.1.

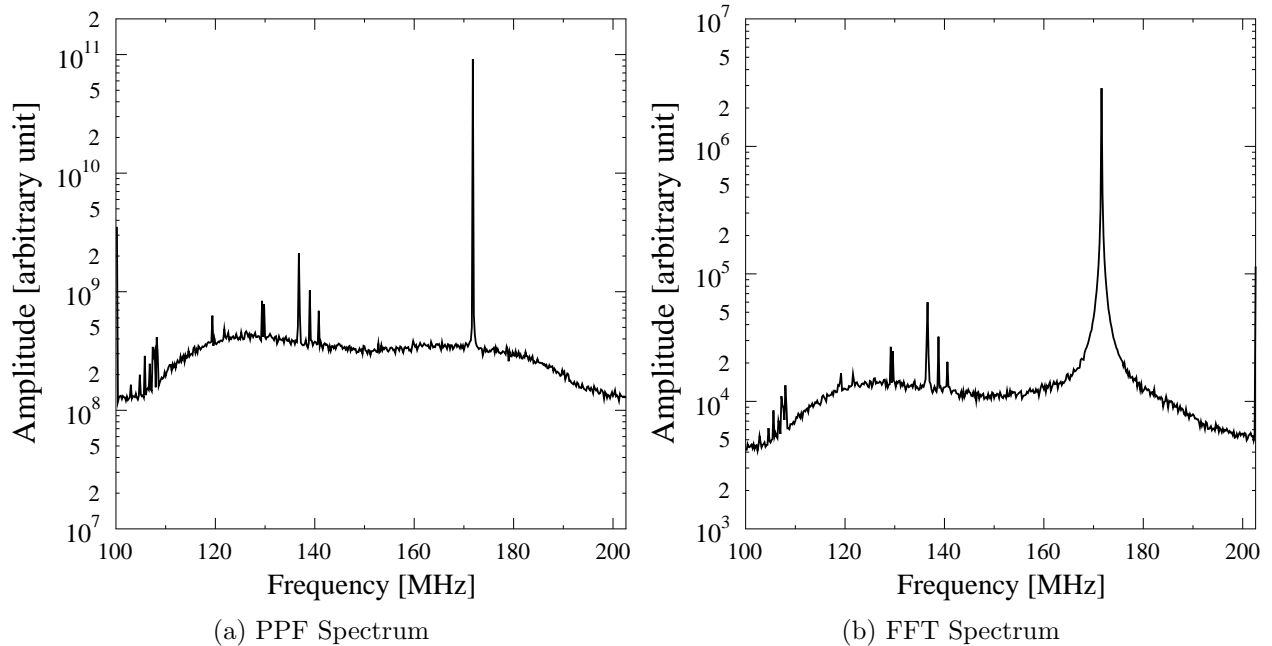


Figure A.23: The frequency spectrum of an HBA tile of LOFAR as determined from the PPF bank is compared with that of a simple FFT.

619 Because the data stream is split into frequency subbands by the PPF, efficient online beam-
 620 forming and STEC-correction is possible. For triggering, we must reconstruct the original
 621 time-domain signal by performing an inversion of the action of the PPF. The PPF inversion
 622 routine (PPF^{-1}) is implemented on CEP (see Fig. 1). Since exact inversion leads to instabilities
 623 the inversion algorithm is based on a Least Mean Squares (LMS) Filter approximation for the
 624 inversion. A LMS Filter is an adaptive filter that adjusts its transfer function according to
 625 an optimized algorithm. The method for FIR inversion is as follows. The filter is provided
 626 with an example of the desired output, together with the corresponding input signal. The filter
 627 then calculates the filter weights (coefficients) that produce the least mean squares fit to the
 628 input signal. In this case, we have calculated the time-domain inversion of an impulse response
 629 (transfer function) for all M sub-filters of the PPF bank.

630 It is computationally expensive to implement the PPF inversion, because it increases the
 631 latency in the online data processing. We have considered using a fewer number of taps in the
 632 PPF inversion in order to to save CPU-processing time. To test this a Nyquist-sampled pulse
 633 was placed at an arbitrary position in a page of 1024 time samples. The PPF transformation
 634 (with 16 taps) and its inversion (with a smaller number of taps) was implemented on the
 635 simulated pulse. Fig. A.24 shows the percentage of power loss in the reconstructed pulse as a
 636 function of position of the simulated pulse in the page. The power of the recovered pulse is
 637 obtained by integrating over 20 time samples. The length of the PPF equals an even number of
 638 pages. Since the signal reconstruction is optimal for a pulse in the center this explains why the
 639 efficiency shown in Fig. A.24 is best near the edges of the page. For the full PPF inversion with
 640 16 taps the power loss is approximately 10% when the pulse is in the center of the page. The
 641 loss strongly increases when the pulse is recovered using a smaller number of taps. For these

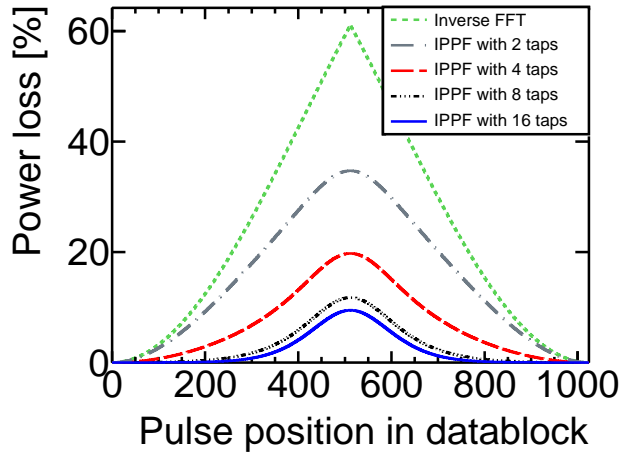


Figure A.24: The power loss for pulse reconstruction as a function of position of short pulse in a data block of 1024 samples. The pulse is reconstructed using a simple inverse FFT (dashed, green), an PPF^{-1} with 2 taps (dotted, green), an PPF^{-1} with 4 taps (long dashed, red), and an PPF^{-1} with 8 taps (dashed-dotted, black) instead of PPF^{-1} of 16 taps (drawn, blue).

642 same pulse-positions, loss approaches 20% for 4 taps, and is nearly 35% for 2 taps. Note that a
 643 simple inverse FFT is equivalent to a PPF^{-1} inversion that is done without applying the inverse
 644 FIR filter function. In this case the power loss reaches 60%. We thus conclude that reducing
 645 the number of taps in the PPF^{-1} inversion routine results in a considerable loss of intensity for
 646 the pulse-response of the system.

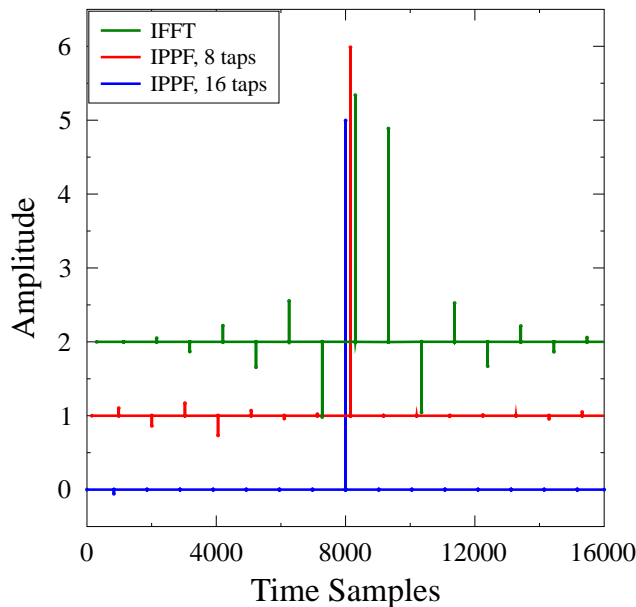


Figure A.25: Inverted delta pulse structure with a simple inverse FFT (green, offset=2), and PPF^{-1} with 8 taps (red, offset=1) instead of PPF^{-1} of 16 taps (blue). The test pulse has amplitude 5. The spectra are also a little offset in time to increase visibility.

647 Because of the initial 16-taps, the PPF strength of a pulse is distributed over 16 output
648 signals. Using the inverse PPF with 16 taps re-combines this information to reproduce the
649 original pulse. If the inversion is performed with fewer taps, or (in the extreme) by perform-
650 ing an inverse FFT, the strength of the original pulse is distributed across multiple echos (see
651 Fig. A.25) which get worse when fewer taps are included in the inversion. It should be noted
652 that the Gaussian noise level stays at the same strength when processed this way. This is be-
653 cause the redistribution of Gaussian noise signals results in both constructive and destructive
654 interference of these noise signals. By contrast, a single sharp, well-defined pulse cannot expe-
655 rience constructive interference with itself, and will only be reduced by reducing the number of
656 taps.

657 References

- 658 [1] R.J. Protheroe and R.W. Clay, *PASA* **21**, 1 (2004).
- 659 [2] V. Berezhinsky *et al.*, *Phys. Rev. D* **81**, 103530 (2010).
- 660 [3] K. Greisen, *Phys. Rev. Lett.* **16**, 748 (1966); G. Zatsepin and V. Kuzmin, *Pis'ma Zh.*
661 *Eksp. Teor. Fiz.* **4**, 114 (1966).
- 662 [4] J. Abraham *et al.*(The Pierre Auger Collaboration), *Nucl. Inst. and Meth. A* **620**, 227
663 (2010). J. Abraham *et al.*(The Pierre Auger Collaboration), *Nucl. Inst. and Meth. A* **613**,
664 29 (2010).
- 665 [5] J. Ahrens *et al.*, *Nucl. Phys. Proc. Suppl.* **118**, 388 (2003).
- 666 [6] P. Gorham *et al.* (ANITA collaboration), *Phys. Rev. D* **82**, 022004 (2010), erratum
667 arXiv:1003.2961
- 668 [7] H. Lehtinen *et al.*, *Phys. Rev. D* **69**, 013008 (2004).
- 669 [8] U. Katz *et al.*, *Nucl. Inst. and Meth. A* **567**, 457 (2006).
- 670 [9] R.D. Dagkesamanskii and I.M. Zheleznyk, *Sov. Phys. J.E.T.P.* **50**, 233 (1989).
- 671 [10] G. Askaryan, *Sov. Phys., J.E.T.P.* **14**, 441 (1962).
- 672 [11] T. Hankins, R. Ekers, and J. O'Sullivan, *Mon.Not.Roy.Astron.Soc.* **283**, 1027 (1996).
- 673 [12] C.W. James, *et al.*, *Mon.Not.Roy.Astron.Soc.* **379**, 1037 (2007).
- 674 [13] P. Gorham *et al.*, *Phys. Rev. Lett.* **93**, 41101 (2004).
- 675 [14] A. Beresnyak *et al.*, *Astron. Rep.* **49**, 127 (2005).
- 676 [15] T.R. Jaeger, R.L. Mutel, K.G. Gayley, *Astropart. Phys.* **34**, 293 (2010).
- 677 [16] O. Scholten *et al.*, *Astropart. Phys.* **26**, 219 (2006).
- 678 [17] O. Scholten *et al.*, *Phys. Rev. Lett.* **103**, 191301 (2009).

- 679 [18] S. Buitink, et al., *A&A* **521**, A47 (2010).
- 680 [19] J.R. Hörandel, et al., *Nucl. Phys. B* **196**, 289 (2009); A. Horneffer, et al.,
681 *Nucl. Inst. and Meth. A* **617**, 482 (2010).
- 682 [20] <http://www.lofar.org/>.
- 683 [21] D. Saltzberg et al., *Phys. Rev. Lett.* **86**, 2802 (2001).
- 684 [22] E. Zas, F. Halzen, and T. Stanev, *Phys. Rev. D* **45**, 362 (1992).
- 685 [23] J. Alvarez-Muñiz and E. Zas, *Phys. Lett. B* **411**, 218 (1997).
- 686 [24] O. Scholten et al., *Nucl. Inst. and Meth. A* **A604**, s102 (2009).
- 687 [25] S. Bevan, *Nucl. Inst. and Meth. A* **604**, S143 (2009).
- 688 [26] J. Abraham, et al. [Pierre Auger Collaboration], *Science* **318** (5852), 938; *Astropart.*
689 *Phys.* **29** (2008) 188.
- 690 [27] J. Abraham, et al. [Pierre Auger Collaboration], *Phys. Rev. Lett.* **101**, 061101 (2008)
- 691 [28] J. Abraham, et al. [Pierre Auger Collaboration], *Astropart. Phys.* **29** (2008) 243; idem
692 **31**, 399 (2009);
- 693 [29] O. Scholten, K. Werner, and F. Ruydy, *Astropart. Phys.* **29**, 94 (2008); Klaus Werner
694 and Olaf Scholten, *Astropart. Phys.* **29**, 393-411 (2008)
- 695 [30] O. Scholten and K. Werner, *Nucl. Instr. and Meth. A* **604**, S24 (2009).
- 696 [31] R. Gandhi, *Nucl. Phys. B* **91**, 453 (2000).
- 697 [32] E. Waxman and J. N. Bahcall, *Phys. Rev.* **D59**, 023002 (1999)
- 698 [33] R. Protheroe and T. Stanev, *Phys. Rev. Lett.* **77**, 3708 (1996)
- 699 [34] V. Barger, P. Huber, D. Marfatia, *Phys. Lett. B* **642**, 333 (2006)
- 700 [35] B. Stappers et al., *accepted for publication A&A*, (2011).
- 701 [36] *Europar*, (2011).
- 702 [37] K. Singh et al., Proc. 31st ICRC, Łódź 2009
- 703 [38] R. Fardon, A.E. Nelson and N. Weiner, *J. Cosmol. Astropart. Phys.* **0410** (2004)005.
- 704 [39] A. Ringwald and L. Schrempp, *J. Cosmol. Astropart. Phys.* **0610** (2006) 012.
- 705 [40] Olaf Scholten and Arjen van Vliet, *J. Cosmol. Astropart. Phys.* **0806**, 015 (2008).
- 706 [41] T. Stanev, astro-ph/0411113 (2004).
- 707 [42] Singh, K. et al., Proc. of 21th ECRS, Slovakia, 2008.

- 708 [43] H. Falcke, *Highlights of Astronomy*, 14, 386, 2007.
- 709 [44] S. K. Mitra, *Digital Signal Processing*, McGraw- Hill, 2001.
- 710 [45] R.J. Nijboer and M. Pandey-Pommier, *Technical Report LOFAR-ASTRON-MEM-251*,
711 (2009); Stefan J. Wijnholds, *Technical Report LOFAR-ASTRON-MEM-205*, (2006).
- 712 [46] S.J. Wijnholds and W.A. van Cappellen, *IEEE Trans. on Antennas and Propagation*, **59**,
713 1981 (2011).
- 714 [47] J. D. Bregman, *Perspectives on Radio Astronomy Technologies for Large Antenna Arrays*
715 , (1999). Proceedings NFRA SKA Symposium on Technologies for Large Antenna Arrays.
716 ASTRON, The Netherlands (1999).
- 717 [48] J. Bray et al, arXiv 1010.1997v1 (Presented at ARENA 2010, Nantes, France 2010)
- 718 [49] <http://nl.wikipedia.org/wiki/C2000>
- 719 [50] S. ter Veen, et al., *Phys. Rev. D* **82**, 103014 (2010).
- 720 [51] J. Abraham et al. [The Pierre Auger Collaboration], *Phys. Lett. B* **685**, 239 (2010).